Appl. Phys. A (2014) 117:1631–1644
DOI 10.1007/s00339-014-8570-5

Applied Physics A
Materials Science & Processing

Understanding the electron-stimulated surface reactions of organometallic complexes to enable design of precursors for electron beam-induced deposition

Julie A. Spencer · Samantha G. Rosenberg · Michael Barclay · Yung-Chien Wu · Lisa McElwee-White · D. Howard Fairbrother

Received: 7 April 2014 / Accepted: 13 June 2014 / Published online: 10 July 2014
© Springer-Verlag Berlin Heidelberg 2014

Abstract Standard practice in electron beam-induced deposition (EBID) is to use precursors designed for thermal processes, such as chemical vapor deposition (CVD). However, organometallic precursors that yield pure metal deposits in CVD often create EBID deposits with high levels of organic contamination. This contamination negatively impacts the deposit's properties (e.g., by increasing resistivity or decreasing catalytic activity) and severely limits the range of potential applications for metal-containing EBID nanostructures. To provide the information needed for the rational design of precursors specifically for EBID, we have employed an ultra-high vacuum (UHV) surface science approach to identify the elementary reactions of organometallic precursors during EBID. These UHV studies have demonstrated that the initial electron-induced deposition of the surface-bound organometallic precursors proceeds through desorption of one or more of the ligands present in the parent compound. In specific cases, this deposition step has been shown to proceed via dissociative electron attachment, involving low-energy secondary electrons generated by the interaction of the primary beam with the substrate. Electron beam processing of the surface-bound species produced in the initial deposition event usually causes decomposition of the residual ligands, creating nonvolatile fragments. This process is believed to be responsible for a significant fraction of the organic contaminants typically observed in EBID nanostructures. A few ligands (e.g., halogens) can, however, desorb during electron beam processing while other ligands (e.g., PF_3, CO) can thermally desorb if elevated substrate temperatures are used during deposition. Using these general guidelines for reactivity, we propose some design strategies for EBID precursors. The ultimate goal is to minimize organic contamination and thus overcome the key bottleneck for fabrication of relatively pure EBID nanostructures.

J. A. Spencer · S. G. Rosenberg · M. Barclay · D. Howard Fairbrother (✉)
Department of Chemistry, Johns Hopkins University, Baltimore, MD 21218, USA
e-mail: howardf@jhu.edu

Y.-C. Wu · L. McElwee-White
Department of Chemistry, University of Florida, Gainesville, FL 32611-7200, USA

1 Introduction

Electron beam-induced deposition (EBID) is a resistless, single-step, vacuum-based, direct-write lithographic strategy that uses a high energy, focused electron beam to stimulate the deposition of metal-containing nanostructures from organometallic precursors transiently adsorbed on a surface (Fig. 1) [1–4]. Primary electrons and/or the secondary electrons, created by the interaction of the primary beam with the substrate, initiate deposition because electron-stimulated decomposition of the precursor produces nonvolatile fragments.

EBID possesses a unique and attractive combination of capabilities for producing three-dimensional nanostructures since the size, shape, and interparticle distance can all be accurately and independently controlled and varied across a range of length scales. EBID also offers a number of advantages compared with other vacuum-based nanofabrication strategies such as ion beam-induced deposition (IBID), electron beam lithography (EBL), and extreme ultraviolet lithography (EUVL) that can also create nanostructures. In particular, EBID can create smaller features than IBID, with less amorphization and without ion

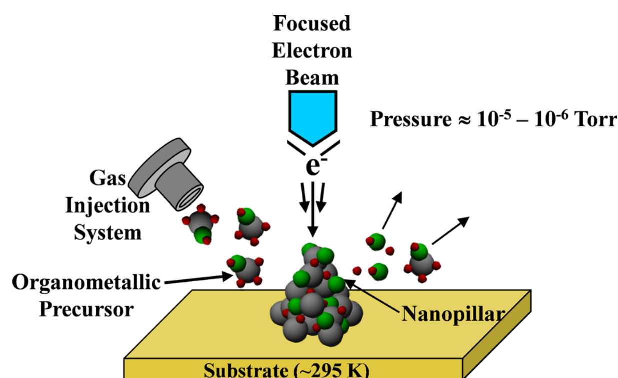

Fig. 1 Schematic representation of a size and shape selected metal-containing nanostructure being deposited by electron beam-induced deposition (EBID)

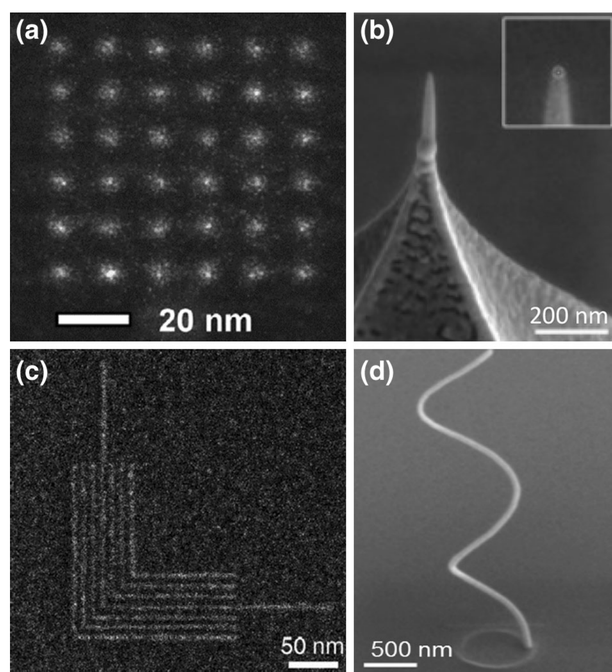

Fig. 2 Structures of different sizes and shapes created by EBID (details in text)

implantation [5–7]. While EBID resolution is comparable to EBL and EUVL [8, 9], it needs no resist layers or etching step for pattern transfer.

A few examples of EBID structures are shown in Fig. 2: An array of platinum-containing dots (approximate diameter 3 nm) deposited from $MeCpPtMe_3$ (Fig. 2a) [10], a platinum-based probe grown on top of a commercially available atomic force microscopy (AFM) cantilever (Fig. 2b) [11], a dense pattern of L-shaped structures deposited from $MeCpPtMe_3$ (Fig. 2c) [12], and a high aspect 3D cobalt nanowire (Fig. 2d) [13]. EBID nanostructures have the potential to act as components in a

Table 1 Precursors developed for CVD that have been used for EBID

Metal	Representative EBID precursors
Au	$Au(acac)Me_2$, $Au(hfac)Me_2$
Cu	$Cu(hfac)_2$, $Cu(hfac)(VTMS)$
Co	Co_2CO_8, $Co(CO)_3NO$
Fe	$Fe(CO)_5$, $Fe(C_5H_5)_2$, $Fe_3(CO)_{12}$
W	$W(CO)_6$, WF_6, WCl_6
Pt	$MeCpPtMe_3$, $Pt(PF_3)_4$, $Pt(hfac)_2$

variety of technologically important applications, some of which have already garnered broad usage, including a commercial system for repairing EUVL masks [14–17], customized tips for local probe microscopes [18, 19], and the fabrication and modification of nanophotonic and nanoplasmonic devices [20–22].

Despite the versatile and attractive capabilities of EBID, and the increasing prominence of electron beam instruments in industry and academia, a number of scientific and technological issues are impeding the further development of EBID as a robust tool for nanofabrication. One of the biggest issues is the low metal content in deposits created from organometallic precursors. For example, structures created from $Au(acac)Me_2$ by EBID exhibit Au contents <20 % [1–3]. Similarly, although pure platinum films can be created by CVD from $MeCpPtMe_3$, EBID structures created from the same precursor have platinum contents <20 % [2, 23, 24]. These EBID deposits/structures typically contain unacceptably high levels of contaminants, particularly carbon and oxygen [25]. These impurities negatively impact the properties of EBID nanostructures because contaminants increase resistivity and adversely affect the electronic structure of the metal atoms in the deposited structures. For example, the resistivity of Pt wires created from $MeCpPtMe_3$ by EBID is typically >1 Ω cm, severely limiting their ability to serve as nanoelectrodes or nanowires [26]. In general, the potential applications for EBID nanostructures as nanowires, catalysts, and biosensors are hindered by the high levels of organic contamination.

The principal reason why EBID structures contain so much residual organic contamination can be traced back to the use of commercially available organometallic precursors, which have been designed to yield pure metallic deposits in thermal deposition processes such as CVD and atomic layer deposition (ALD). Table 1 shows a representative list of CVD precursors that have been used in EBID to deposit metal-containing nanostructures. However, during EBID, precursor ligands that dissociate

thermally during CVD are susceptible to electron-stimulated decomposition, leading to contamination in the deposited material [2].

The low metal content that characterizes the chemical composition of EBID nanostructures created from existing CVD precursors highlights the need to develop new precursors designed to produce high metal content in EBID nanostructures. Precedent for the value of a targeted synthetic approach can be found in the ability of EBID to deposit pure nanocrystalline gold from PF_3AuCl, a precursor synthesized specifically for EBID [27, 28]. Unfortunately, PF_3AuCl is sensitive to temperature, air, moisture, and light, with an effective storage lifetime of a few days, rendering it impractical for routine EBID. This example does, however, illustrate the underlying motivation for this methodology: specifically, that the synthesis and evaluation of new precursors could enable EBID to deposit size and shape selected nanoparticles with significantly improved metal content and a corresponding greater range of applications.

1.1 An ultra-high vacuum surface science approach to EBID

In contrast to CVD and ALD, where a substantial body of mechanistic work underlies precursor design [29, 30], there is a lack of information on the molecular events that accompany EBID. However, recent ultra-high vacuum (UHV) surface science studies have begun to provide information useful in formulating design strategies for EBID precursors (see Fig. 3) [31–38]. In contrast to studies conducted in electron microscopes, where deposits are created under steady state deposition conditions, the UHV surface science approach relies on studying the effect of electron irradiation on nanometer thick films of precursor molecules adsorbed onto chemically inert substrates at low temperatures. Surface analytical tools such as X-ray photoelectron spectroscopy (XPS) and reflection absorption infrared spectroscopy (RAIRS) can follow changes in the surface composition and bonding environment of the various elements within the precursor molecule, complemented by mass spectrometry (MS) which can detect the volatile species ejected from the film as a consequence of electron-stimulated reactions. The UHV environment ($P_{base} < 5 \times 10^{-9}$ Torr) simplifies data interpretation by ensuring that the effects of electron irradiation on adsorbed precursor molecules can be studied without the complicating effects of contaminants (water or hydrocarbons) typically present in electron microscopes ($P_{base} \approx 10^{-5}$–10^{-6} Torr regime). Furthermore, the low background pressure allows mass spectrometry (MS) to identify gas phase products produced during EBID. This information cannot be obtained in typical EBID experiments due to the

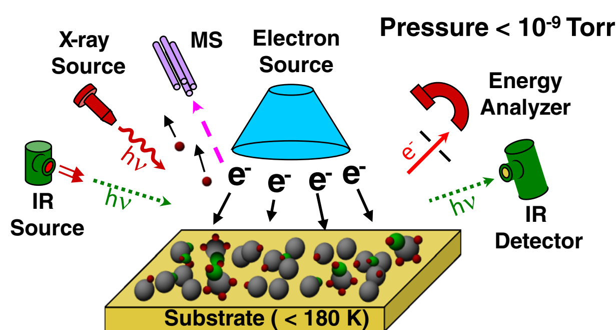

Fig. 3 Schematic representation of the ultra-high vacuum surface science approach to study EBID precursors

higher base pressure as well as the presence of a constant partial pressure of precursor molecules during deposition. Compared to the typical EBID experiments (Fig. 1) performed in electron microscopes, the UHV surface science approach (Fig. 3) also allows the effects of electron irradiation on adsorbed precursors to be interrogated in situ, and as a function of electron dose. This provides a route to obtain information that can be used to develop a molecular level understanding of EBID.

Evidence for the existence of structure–activity relationships in EBID can be found in MS studies where the volatile carbon-containing species created during electron irradiation of adsorbed organometallic complexes exhibit a systematic dependence on the ligand architecture (Fig. 4) [34]. In some instances, this information can be directly related to the chemical composition of EBID depositions. For example, electron irradiation of $Ni(MeCp)_2$ (Fig. 4a) produces nonvolatile carbon-containing products, suggesting that η^5-cyclopentadienyl ligands will be inappropriate for EBID precursors. Consistent with this idea, high carbon contents are observed for EBID structures created from organometallic precursors containing η^5-cyclopentadienyl ligands [2, 23, 24, 39]. In the case of $Co(CO)_3NO$ (Fig. 4f), CO is the dominant gas phase species produced during electron irradiation, with little NO observed. This observation helps to explain why EBID deposits created from $Co(CO)_3NO$ have much higher N/C ratios than the 1:3 ratio present in the precursor [40–45].

Figure 5 describes the elementary steps that we believe underpin the EBID process. In a typical EBID experiment, conducted in an electron microscope and under a constant partial pressure of precursor molecules, the adsorbed precursor molecules ($ML_{n(ads)}$) are in equilibrium with gas phase species ($ML_{n(g)}$). Results from our UHV surface science studies have shown that the subsequent reactions of the adsorbed precursor during the EBID process can be broken down into a number of sequential steps: An initial electron-stimulated deposition event followed by either

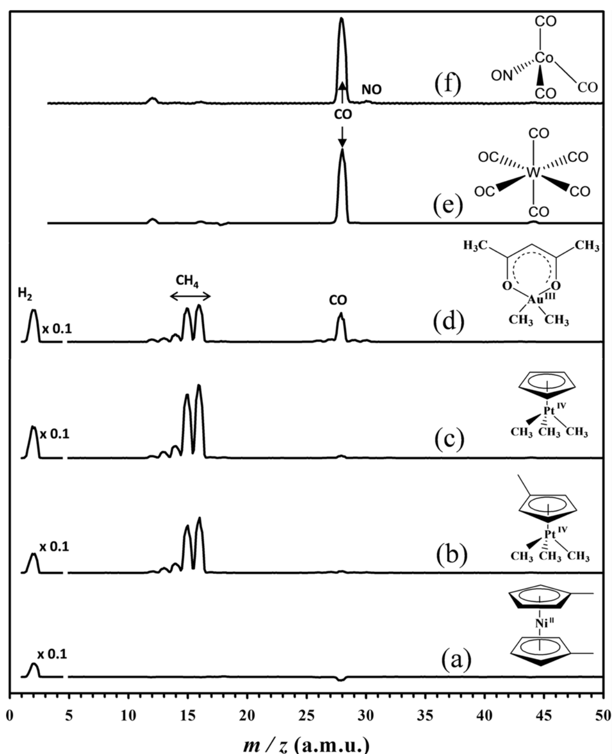

Fig. 4 Mass spectra of the volatile species produced when six different organometallic precursors, adsorbed onto gold substrates, were irradiated by 500 eV electrons. (*a*) $Ni(MeCp)_2$, (*b*) $MeCpPtMe_3$, (*c*) $CpPtMe_3$, (*d*) $Au(acac)Me_2$, (*e*) $W(CO)_6$, (*f*) $Co(CO)_3NO$

electron or thermal processing of the adsorbed species created in the initial step [35].

1.1.1 Initial electron-stimulated (deposition) step

The initial electron interaction converts adsorbed parent precursor molecules ($ML_{n(ads)}$) into a nonvolatile species that is now bound to the substrate. From now on, this will be referred to as the initial deposition step. Our

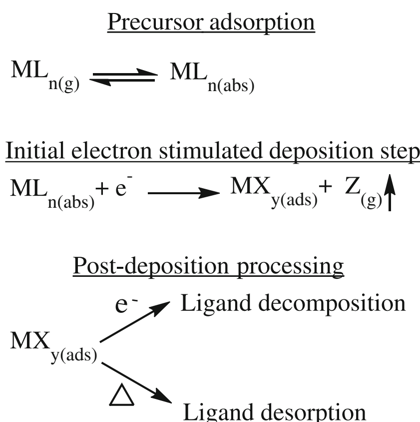

Fig. 5 Elementary reaction steps that underpin the EBID process

studies have shown that this initial step is accompanied by desorption of volatile fragments [32, 36–38]. In the case of organometallic complexes with monodentate ligands (e.g., $W(CO)_6$, $Pt(PF_3)_4$, $Co(CO)_3NO$, $MeCpPtMe_3$), these gas phase species are typically intact ligands which have dissociated from the parent molecule. This process can be represented by the following general expression:

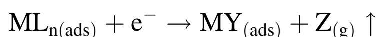

$$ML_{n(ads)} + e^- \rightarrow MY_{(ads)} + Z_{(g)} \uparrow$$

where $MY_{(ads)}$ represents the nonvolatile species that is now bound to the substrate after the organometallic precursor ML_n decomposes, and $Z_{(g)}$ represents the volatile fragments released [35–38]. Information on the deposition step can be acquired from data obtained when the adsorbed precursor molecules are initially exposed to electrons, corresponding to comparatively short electron doses (electron dose = (electron flux × time)/surface area, $e^- \, cm^{-2}$).

The ability of the UHV surface science approach to elucidate the initial bond breaking step for different precursors will be illustrated by considering results obtained on two platinum-containing precursors, $MeCpPtMe_3$ and $Pt(PF_3)_4$ [32, 38].

1.1.1.1 MeCpPtMe₃

Trimethyl(methylcyclopentadienyl)-platinum(IV) ($MeCpPtMe_3$) is one of the most common precursors used to create conductive nanostructures/nanowires [23, 24, 26, 31, 46–52]. XPS data from UHV surface science experiments shown in Fig. 6 demonstrate that when nanometer thick films of $MeCpPtMe_3$ are exposed to electrons, the C/Pt ratio decreases by ≈11 % of its initial value, creating films that contain 89 % carbon and 11 % platinum [32]. This change in stoichiometry can be accurately determined by integrating the area of the Pt(4f) and C(1s) peaks observed by XPS before and after electron irradiation. This highlights a notable advantage of the low-temperature UHV surface science approach; specifically, the ability to directly measure the film's composition before and after electron irradiation, facilitating an accurate determination of even relatively small changes in film composition. The significance of this decrease in the ratio of carbon to platinum atoms (C/Pt) is that since the parent molecule contains one central Pt atom and nine C atoms, a decrease of ≈11 % corresponds to the loss of exactly one carbon atom from the parent molecule as a result of the electron-induced deposition step [32]. Complementary MS data (Fig. 4) reveal that this carbon atom is released from the adsorbed layer as methane during irradiation, irrespective of whether $MeCpPtMe_3$ or its derivative, $CpPtMe_3$ is used. Collectively, these XPS and MS results point to an initial electron-stimulated deposition process that proceeds through the cleavage of one of the Pt–CH_3 bonds, with the

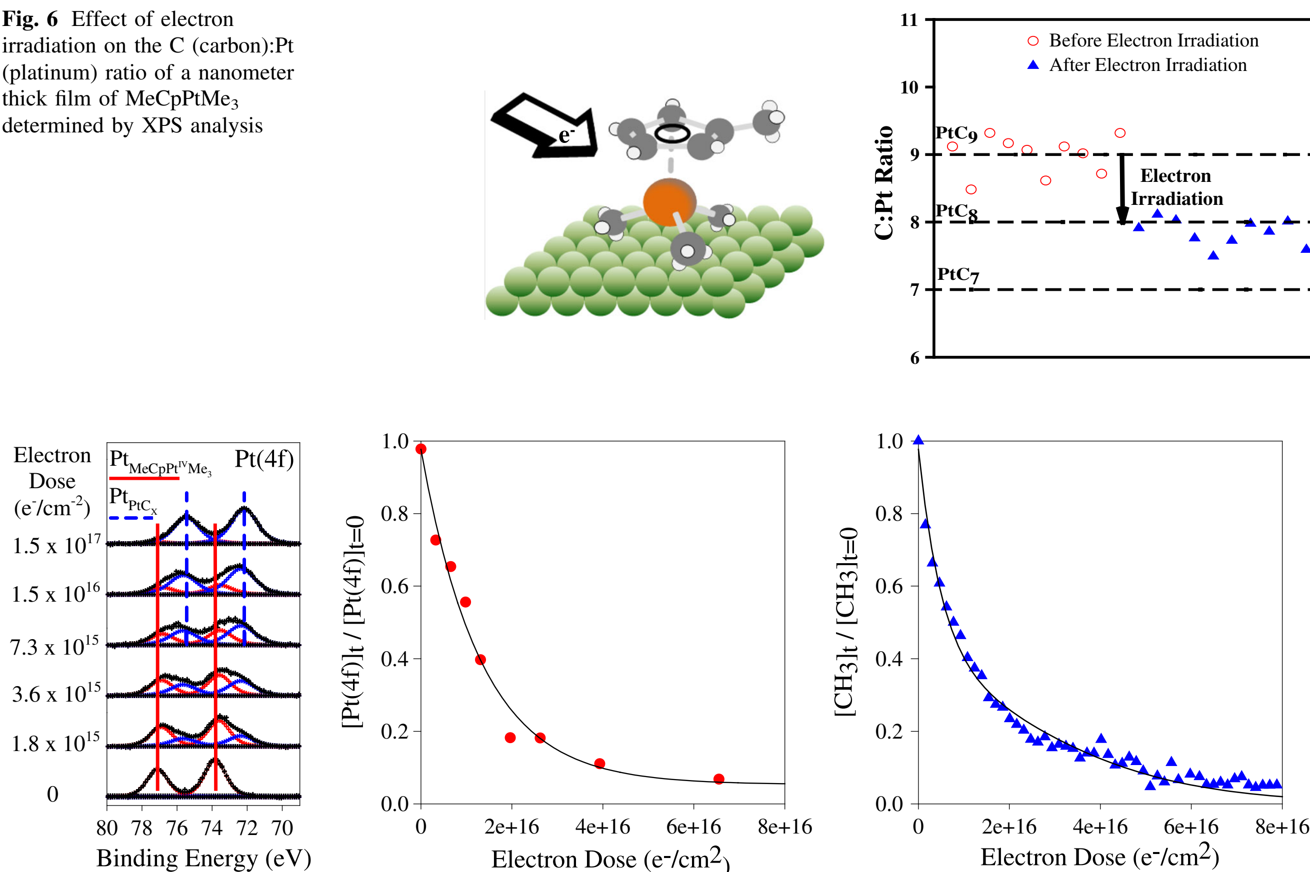

Fig. 6 Effect of electron irradiation on the C (carbon):Pt (platinum) ratio of a nanometer thick film of $MeCpPtMe_3$ determined by XPS analysis

Fig. 7 Effect of electron irradiation on adsorbed $MeCpPtMe_3$ molecules: *Left-hand panel* Evolution of the Pt(4f) region; *Middle panel* Kinetics of Pt(IV) reduction based on Pt(4f) region; *Right-hand panel* Kinetics of CH_3/CH_4 evolution

remaining carbon atoms becoming trapped in the deposit that forms [32].

Corresponding XPS data acquired on the Pt(4f) region (Fig. 7 (left-hand panel)) show that electron irradiation converts the Pt(IV) species in the parent $MeCpPtMe_3$ molecules into a reduced Pt species (Pt_{red}). Because of the significant change in formal oxidation state involved in this process, the Pt(4f) binding energy difference between the Pt(IV) and Pt_{red} species is on the order of 2 eV. This facilitates an accurate spectral deconvolution of the Pt(4f) region and enables the rate of reaction to be determined [Fig. 7 (middle panel)]. The right-hand panel in Fig. 7 shows that the rate of methane/methyl radical production (monitored by the $m/z = 15$ fragment) is, within experimental error, equal to the rate of Pt(IV) reduction (Fig. 7 (middle panel)). This demonstrates that the cleavage of one of the Pt–CH_3 bonds is involved in the initial deposition step [32]. Comparisons with gas phase studies on the low-energy electron interactions with $MeCpPtMe_3$ [53] also allow us to conclude that this initial deposition step proceeds via a dissociative electron attachment (DEA) step involving low-energy (<10 eV) electrons generated by the interaction of the high-energy primary beam with the substrate. Consequently, the initial deposition step can be represented by Fig. 8 and the following equation:

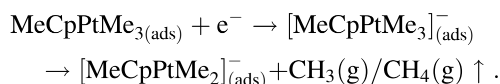

$$MeCpPtMe_{3(ads)} + e^- \rightarrow [MeCpPtMe_3]^-_{(ads)} \rightarrow [MeCpPtMe_2]^-_{(ads)} + CH_3(g)/CH_4(g)\uparrow .$$

1.1.1.2 $Pt(PF_3)_4$ Tetrakis(trifluorophosphine)platinum is a carbon-free precursor, although EBID structures generated from $Pt(PF_3)_4$ are typically dominated by phosphorus contamination [24, 54–57]. XPS data (shown in Fig. 9) show the effect of comparatively short irradiation times (electron doses $<1.5 \times 10^{15}$ e^-/cm^2) on nanometer thick films of $Pt(PF_3)_4$ adsorbed on amorphous carbon substrates [38]. A determination of the dissociation mechanism relies on analyzing how the relative atom concentration and speciation of the elements contained within the ligands change under the influence of electron irradiation. During this initial period of irradiation, Fig. 9 shows that phosphorus and fluorine atoms are lost from the adsorbate layer [38]. By integrating the spectral intensity within the P(2p) and F(1s) regions for multiple $Pt(PF_3)_4$ films exposed to

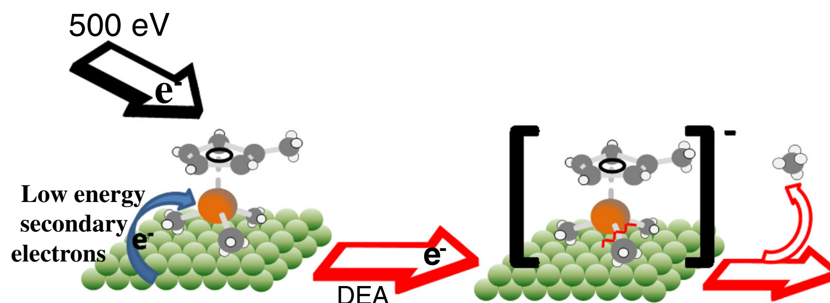

Fig. 8 Electron-stimulated decomposition of $MeCpPtMe_3$. The incident primary beam creates low-energy secondary electrons from the substrate, which subsequently attach to adsorbed $MeCpPtMe_3$ molecules to form a negative ion. These unstable species falls apart via a dissociative electron attachment (DEA) process through the cleavage of one Pt–CH_3 bond and the release of CH_3/CH_4

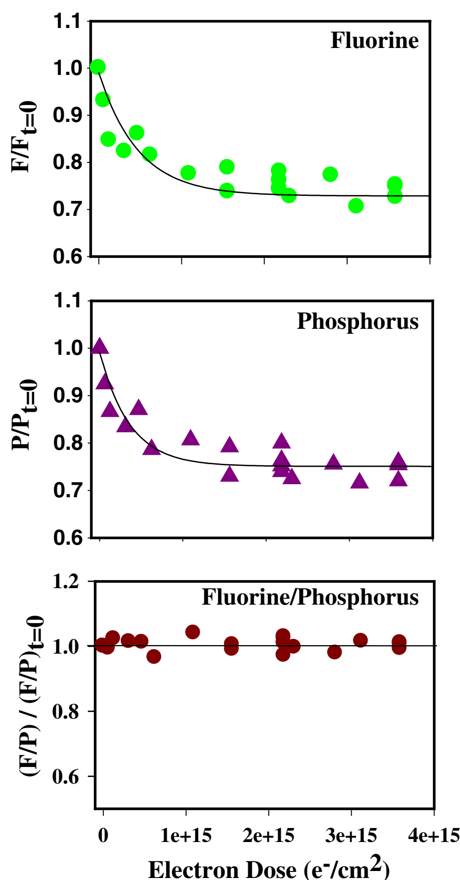

Fig. 9 Changes in the fractional coverages (of phosphorus ($P/P_t = 0$), fluorine ($F/F_t = 0$), and the ratio of fluorine/phosphorus (F/P) atoms for $Pt(PF_3)_4$ films exposed to comparatively small electron doses ($<4 \times 10^{15}$ e^-/cm^2)

electron doses $<1.5 \times 10^{15} e^-/cm^2$, Fig. 9 reveals that during this period of irradiation the concentration of adsorbed phosphorus and fluorine atoms both decrease to 75 % of their initial values [38]. Moreover, the rate of electron-stimulated phosphorus and fluorine atom loss is the same, causing the ratio of phosphorus to fluorine atoms remaining in the film to remain constant (bottom panel in Fig. 9). Collectively, these observations indicate that the initial step in the decomposition of adsorbed $Pt(PF_3)_4$ molecules proceeds via cleavage of one of the metal–ligand bonds and loss of one PF_3 group [38]. A comparison of gas phase and surface science studies leads to the same conclusion as for $MeCpPtMe_3$; notably, that dissociation of adsorbed $Pt(PF_3)_4$ precursor molecules in EBID occurs via a DEA process, with the low-energy electrons being produced by the interaction of the primary beam with the substrate [38, 58]. The overall deposition process can be represented by the following equation,

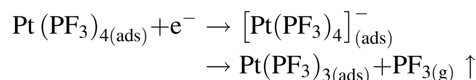

$$\mathrm{Pt}\left(\mathrm{PF}_3\right)_{4(\mathrm{ads})} + e^- \rightarrow \left[\mathrm{Pt}(\mathrm{PF}_3)_4\right]^-_{(\mathrm{ads})} \rightarrow \mathrm{Pt}(\mathrm{PF}_3)_{3(\mathrm{ads})} + \mathrm{PF}_{3(\mathrm{g})} \uparrow$$

shown schematically in Fig. 10.

Similar UHV surface science studies have also been conducted on $W(CO)_6$ and $Co(CO)_3NO$, two other popular EBID precursors. Table 2 summarizes the initial deposition steps elucidated from our UHV surface science studies on all of the organometallic complexes studied so far.

1.1.2 Post-deposition processing

Following the initial deposition step, a metal-containing fragment, MY(s), is left bound on the surface. For some organometallics, the initial ligand ejection step precipitates a reaction within the remaining ligands. For example, CO is ejected from $Co(CO)_3NO$ simultaneously with the decomposition of the surface-bound NO ligand [37]. However, the fate of most $MY_{(ads)}$ species left behind on the surface is determined by the effects of subsequent electron or thermal processing [35].

Experimentally, an advantage of the UHV surface science approach over traditional EBID experiments performed in electron microscopes is that the effect of both electron and thermal processing on different $MY_{(ads)}$ species created from various EBID precursors can be studied independently [35]. This can be accomplished in a two-step

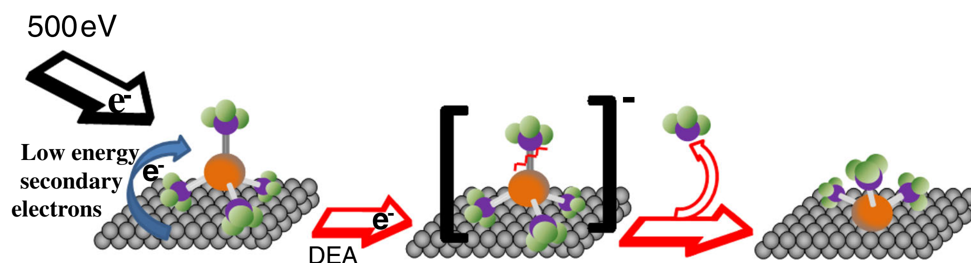

Fig. 10 Summary of the electron-induced deposition step for $Pt(PF_3)_4$. The incident primary beam creates low-energy secondary electrons from the substrate, which subsequently attach to adsorbed $Pt(PF_3)_4$ molecules to form a negative ion which falls apart via a dissociative electron attachment (DEA) process through the cleavage of one Pt–PF_3 bond and the release of a single PF_3 ligand

Table 2 Summary of the initial electron-induced deposition step for several types of organometallic precursors

Organometallic Precursor	$MX_{(ads)}$ - Proposed	+	$Y_{(g)}$ ↑
(MeCp)M(CH_3)$_3$: M, CH_3, CH_3, CH_3	(MeCp)M: H_3C, M, H_3C	+	$CH_3/CH_{4(g)}$ ↑
M(PF_3)$_4$: PF_3, M, F_3P, PF_3, PF_3	F_3P, F_3P, PF_3, M	+	$PF_{3(g)}$ ↑
M(CO)$_6$: CO, OC, CO, OC, M, CO, CO	OC, CO, OC—M—CO; OC, M, CO; OC, CO, OC, CO, M, CO	+	$nCO_{(g)}$ ↑ (n=2.0-2.5)
M(CO)$_3$(NO): CO, M, OC, CO, ON	CO, OC, CO, N^{3-}, M, O^{2-}, M, O^{2-}, N^{3-}	+	$nCO_{(g)}$ ↑ (n=1.0-1.5)

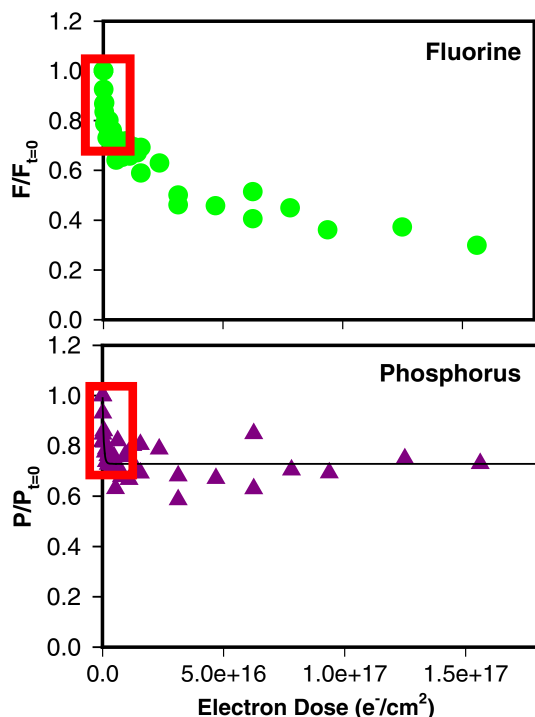

Fig. 11 Changes in the fractional coverages (of phosphorus ($P/P_{t=0}$) and fluorine ($F/F_{t=0}$) for $Pt(PF_3)_4$ films exposed to larger electron doses ($>4 \times 10^{15}$ e^-/cm^2). The red box indicates the initial period of electron irradiation described in Fig. 9

process. First, the organometallic precursor must be pre-exposed to an electron dose that is just enough to ensure that all of the molecules have undergone the initial deposition step ($ML_{n(ads)} + e^- \rightarrow MY_{(ads)} + Z_{(g)}\uparrow$). Knowledge of the kinetics and nature of the initial deposition step is therefore a necessary prerequisite to studying the effects of post-deposition processing. Once the $MY_{(ads)}$ has been created on the surface using the controlled electron dose, the substrate is either: (1) exposed to additional electrons to examine electron processing ($MY_{(ads)} + e^- \rightarrow ?$) or (2) annealed to increasing temperatures to investigate thermal processing ($MY_{(ads)} + \Delta \rightarrow ?$). In either case, the fate of the $MY_{(ads)}$ species can be determined in situ using surface analytical techniques, principally XPS [35].

1.1.3 Electron processing

In typical EBID experiments conducted in electron microscopes at ambient temperatures, $MY_{(ads)}$ species will invariably be subject to a large degree of electron processing due to the extremely high electron fluxes [1–4]. Under these deposition conditions, experimental evidence suggests that ligand *decomposition* rather than *desorption* dominates [32, 36–38]. For example, the XPS data shown in Fig. 11 reveal that electron irradiation of the $Pt(PF_3)_3$ intermediate produced in the initial deposition of $Pt(PF_3)_4$

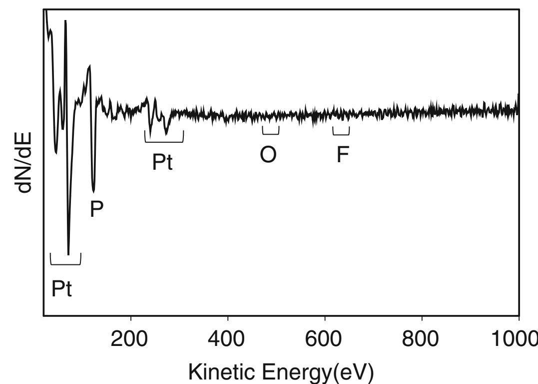

Fig. 12 Auger electron spectra (AES) of an EBID deposit created in a UHV chamber under steady state deposition conditions from $Pt(PF_3)_4$

leads to a sustained decrease in the concentration of adsorbed fluorine atoms, while the phosphorus content in the film remains constant at 75 % of its initial value [38]. These observations indicate that electron processing of adsorbed $Pt(PF_3)_3$ species does not cause PF_3 ligand ejection, but instead decomposes the PF_3 ligands by P–F bond cleavage, ejecting fluoride ions into the gas phase, thus:

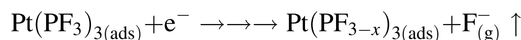

$$Pt(PF_3)_{3(ads)} + e^- \rightarrow\rightarrow\rightarrow Pt(PF_{3-x})_{3(ads)} + F^-_{(g)} \uparrow$$

Ultimately, this leads to the retention of residual phosphorus atoms in the deposit. This explains why EBID deposits created from $Pt(PF_3)_4$ are typically dominated by platinum and phosphorus atoms [54–57, 59]. Indeed, we have generated an EBID structure in an Auger electron spectrometer, under steady state deposition conditions and an electron flux that closely mimic those used in electron microscopes, that contains only platinum and phosphorus atoms (see Fig. 12) [38].

In the case of $MeCpPtMe_3$, experimental evidence suggests that the intermediate produced by the initial Pt–CH_3 bond cleavage event releases hydrogen as a result of electron-stimulated C–H bond cleavage, ultimately producing platinum atoms encased in a carbonaceous matrix with an average stoichiometry of $PtC_{8(ads)}$ [32]. Thus, except for the single carbon atom lost during the deposition step, the remaining carbon atoms remain trapped in the deposit. This helps to rationalize the experimental observation that EBID nanostructures generated from $MeCpPtMe_3$ contain only 10–20 % atomic concentration of platinum atoms [2, 23, 24].

For metal carbonyls, MS and XPS data indicate that the initial deposition step proceeds via CO desorption, although multiple CO groups can be released [36, 37]. However, subsequent electron-stimulated reactions of the remaining partially decarbonylated fragments induce

decomposition of the residual CO ligands, producing graphitic carbon and reactive oxygen species that often react with the central metal atom to form a metal oxide [36, 37]. The overall process can be represented as

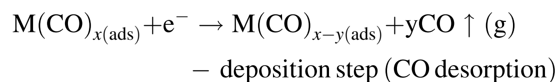

$$M(CO)_{x(ads)} + e^- \rightarrow M(CO)_{x-y(ads)} + yCO \uparrow (g) \quad \text{– deposition step (CO desorption)}$$

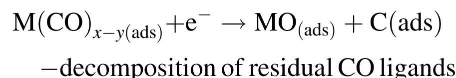

$$M(CO)_{x-y(ads)} + e^- \rightarrow MO_{(ads)} + C(ads) \quad \text{–decomposition of residual CO ligands}$$

Hence, although electron irradiation initiates ligand desorption from the molecular precursor ($ML_{(ads)}$) in step 1, electron processing of the residual ligands left behind in the $MY_{(ads)}$ species is responsible for ligand decomposition. We believe that this second step is the primary source of organic contamination in EBID structures. One notable exception is metal–halogen bonds that are susceptible to electron-stimulated halide ion desorption of the general form,

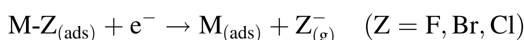

$$M\text{-}Z_{(ads)} + e^- \rightarrow M_{(ads)} + Z^-_{(g)} \quad (Z = F, Br, Cl)$$

An important consequence of this reaction channel is that halogen atoms directly attached to the central metal atom in organometallic complexes could be scrubbed by electron processing. However, the addition of halogen atoms to organometallic complexes typically decreases their volatility, an important practical requirement for an EBID precursor.

1.1.4 Thermal processing

From some $MY_{(ads)}$ species generated in the initial deposition event, thermal processing represents an alternative to the electron processing described in the previous section. The importance of this reaction pathway is that *thermal reactions are often characterized by ligand desorption as opposed to ligand decomposition*. Consequently, thermal processing of $MY_{(ads)}$ species can significantly decrease the level of organic contamination within the final deposit, with corresponding improvements in metal purity [35, 60]. However, there are some important limitations to the value and practical utility of thermal processing in EBID. Not every ligand undergoes thermal desorption, and even if the ligands do desorb, elevated substrate temperatures are typically needed, requiring the presence of a heated sample stage in the electron microscope. If a heated stage is used, the substrate temperature during deposition must always be lower than the onset temperature for CVD to prevent conformal deposition. Moreover, in typical EBID experiments conducted under steady state deposition conditions in electron microscopes, any potentially positive effects of thermal processing will always have to compete with the generally deleterious effects of electron processing.

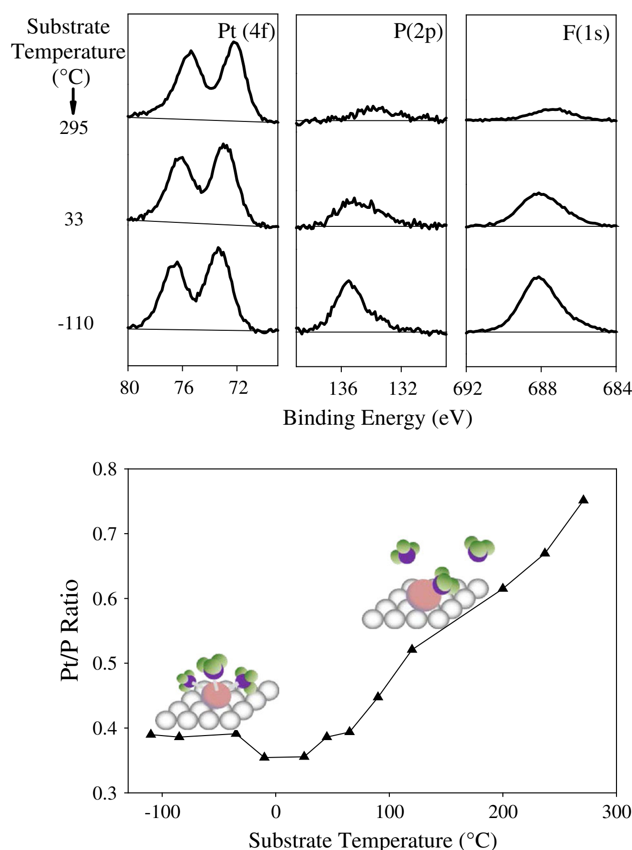

Fig. 13 Influence of substrate temperature on $Pt(PF_3)_{3(ads)}$ species: (*top*) Pt(4f), P(2p) and F(1s)XPS regions and (*bottom*) Pt/P ratio

One precursor that exemplifies the positive effect of using elevated substrate temperatures during deposition is $Pt(PF_3)_4$. In this case, thermal desorption of PF_3 ligands from the $Pt(PF_3)_3$ intermediate can occur at substrate temperatures only slightly above room temperature. Experimentally, this information was acquired by exposing thin films of $Pt(PF_3)_4$ to an electron dose ($<6 \times 10^{15}$ e^-cm^{-2}), a value large enough to create $Pt(PF_3)_{3(ads)}$ species, but insufficient to induce any significant P–F bond cleavage [35]. Figure 13 demonstrates the effect of annealing a film, composed predominantly of $Pt(PF_3)_{3(ads)}$ species, and shows that increasing the substrate temperature above room temperature leads to a decrease in the concentration of phosphorus and fluorine atoms, while the Pt signal and the P/F ratio (not shown) remain relatively constant [35]. This is consistent with the thermal desorption of PF_3 ligands from the $Pt(PF_3)_{3(ads)}$ intermediate ($Pt(PF_3)_{3(ads)} + \Delta \rightarrow PF_{3(g)}\uparrow$), which is responsible for the increase in the Pt/P ratio shown in Fig. 13 at elevated temperatures. Consistent with this assertion, the degree of phosphorus contamination in EBID deposits created from $Pt(PF_3)_4$ under steady state deposition conditions on a heated substrate has been shown to decrease dramatically

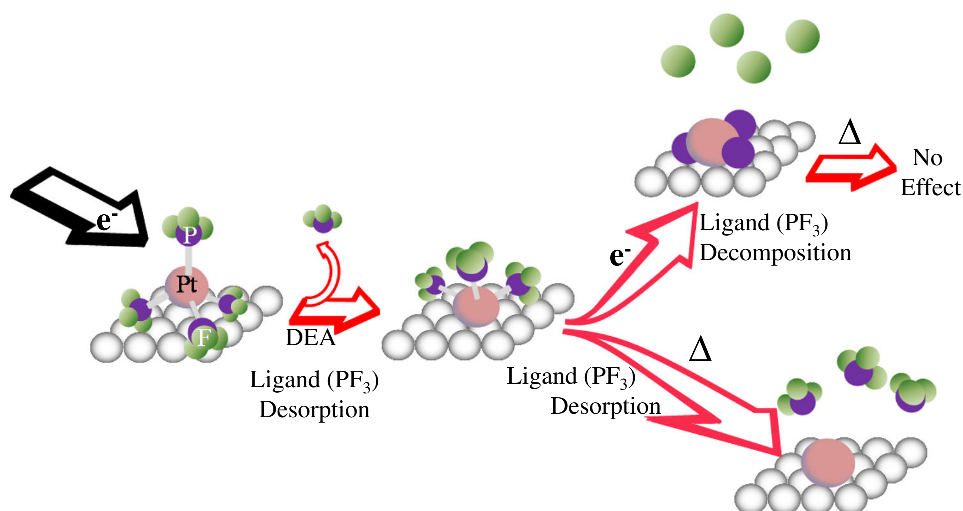

Fig. 14 Summary of the molecular level events that occur during the EBID of $Pt(PF_3)_4$

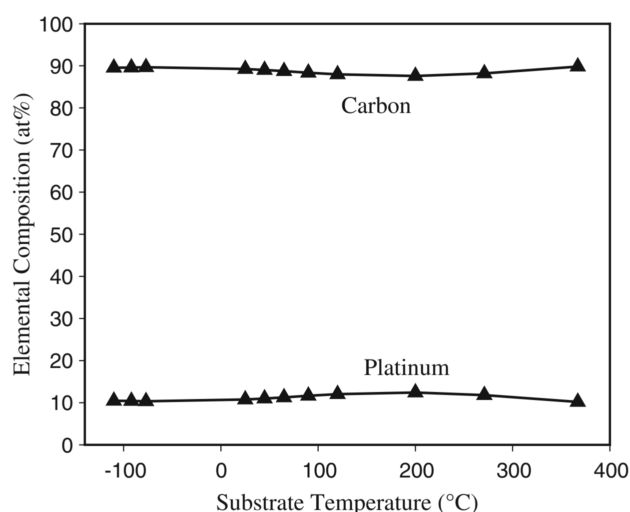

Fig. 15 Effect of substrate temperature on the chemical composition of EBID films created from $MeCpPtMe_3$

when the substrate temperature is raised to only 100 °C during deposition [57].

The effect of thermal processing is therefore to decrease the level of phosphorus contamination. In contrast, electron processing of the same $Pt(PF_3)_{3(ads)}$ intermediate leads to PF_3 decomposition and the formation of nonvolatile phosphorus atoms [35]. Figure 14 shows the overall sequence of elementary reaction steps that can occur during $Pt(PF_3)_4$ EBID.

However, not all ligands or ligand architectures benefit from thermal processing. Figure 15 shows the effect of annealing a $MePtCpMe_3$ film that was initially exposed to an electron dose of 3.37×10^{16} $e^- cm^{-2}$, an electron dose just sufficient to effect Pt–CH_3 bond cleavage in all of the adsorbed $MeCpPtMe_3$ molecules [35]. Analysis of Fig. 15 reveals that the film's chemical composition is invariant to the substrate temperature in the range −110 to 367 °C, remaining at ≈90 % carbon and ≈10 % platinum. This indicates that following the initial Pt–CH_3 bond cleavage event that characterizes the deposition step, all of the remaining carbon atoms become incorporated into the deposit [35]. In this instance, results of the UHV surface science studies can be directly compared with data obtained by Mulders et al. [60] who also found that the chemical composition of EBID films created from $MeCpPtMe_3$ in an SEM was invariant to the substrate temperature between 25 and 360 °C. Thus, there is no advantage to using elevated substrate temperatures for the $MeCpPtMe_3$ precursor. This underlines the need to avoid η^5-cyclopentadienyl ligands in any precursor designed specifically for EBID.

A summary of the different ways in which $MY_{(ads)}$ species are processed by either electrons or thermal reactions is shown in Table 3 [31–38].

2 Precursor design strategies for EBID

Based on the insights from UHV surface science studies, the ideal EBID precursor should have a small number of ligands including ones that have been shown capable of desorbing: (1) as neutral molecules (e.g., CO) in the initial deposition step, (2) by thermal processing at elevated substrate temperatures (e.g., PF_3) or (3) as a result of electron processing (halogens in metal–halide complexes). In the following section, we describe how this information could be used in the design of EBID-specific precursors, using Au- and Pt-containing organometallic complexes as representative examples.

2.1 Strategies for Au precursors

The two Au(I) compounds that have been used successfully in prior studies of gold EBID: $ClAu(PF_3)$ [27, 28] and

Table 3 Summary of the electron (e^-) and thermal (Δ) processing routes for $MY_{(ads)}$ intermediates produced by different organometallic precursors in the initial electron-induced deposition step

Intermediate	e^-	Δ
Cp–M, H_3C, H_3C	MC_9 + $H_{2(g)}$ ↑	MC_9 + $H_{2(g)}$ ↑
F_3P, F_3P, PF_3, M	MP_3 + $F^-_{(g)}$ ↑	M + $3PF_{3(g)}$ ↑
OC, CO, OC—M—CO	M_xO_b C	M C M_xO_b + $CO_{(g)}$ ↑
H, C	C + $H_{2(g)}$ ↑	C + $H_{2(g)}$ ↑
X, M	M + $X^-_{(g)}$ ↑	M + $X_{2(g)}$ ↑
X = halogen; X, C	C + $X^-_{(g)}$ ↑	C + $X_{2(g)}$ ↑

ClAuCO [61] are both of the type XAuL, featuring one halide ligand X and one strongly π-acidic neutral two-electron donor ligand (L = CO, PF_3) which is stable as a gas phase species. We hypothesize that XAuL provides an optimal framework to create organometallic precursors capable of depositing pure Au by EBID via the following reaction sequence:

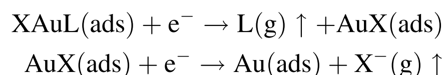

$$XAuL(ads) + e^- \rightarrow L(g) \uparrow + AuX(ads)$$
$$AuX(ads) + e^- \rightarrow Au(ads) + X^-(g) \uparrow$$

This sequence of proposed reaction steps is based on the observations that both CO and PF_3 ligands can be ejected as gas phase species in the initial deposition step, coupled with the susceptibility of metal–halogen bonds toward electron-stimulated halide desorption.

Although $ClAu(PF_3)$ [27, 28] and ClAuCO [61] have both been used to deposit gold structures of fairly high purity, the sensitivity of these compounds toward temperature, air, moisture, and light renders both impractical for storage and scale-up to the quantities needed for any kind of practical applications. In addition to being stable, viable precursors must also be suitably volatile for a vacuum-based deposition process such as EBID. Guided by these basic chemical and physical requirements, a reasonable approach to precursor design would begin with $ClAu(PF_3)$ and ClAuCO as lead compounds and vary the coordination sphere using ligands that are isoelectronic to those in $ClAu(PF_3)$ and ClAuCO but chosen to impart stability to the compounds without compromising volatility. Some possible strategies for generating a small library of precursor candidates are illustrated in Fig. 16.

As an example, since $ClAu(PF_3)$ is well characterized [62, 63], one possible approach is to make derivatives of the phosphine ligand that still contain two of the three P–F bonds to maintain the ligand's overall π-acidic character (Fig. 16) [64], but with a new P–R bond that has the potential to improve precursor stability and thus suitability for EBID. This approach is supported by the successful synthesis of $ClAuPF_2R$ complexes [65], although no EBID studies with these organometallic precursors have been reported. An example of the dependence of stability on the

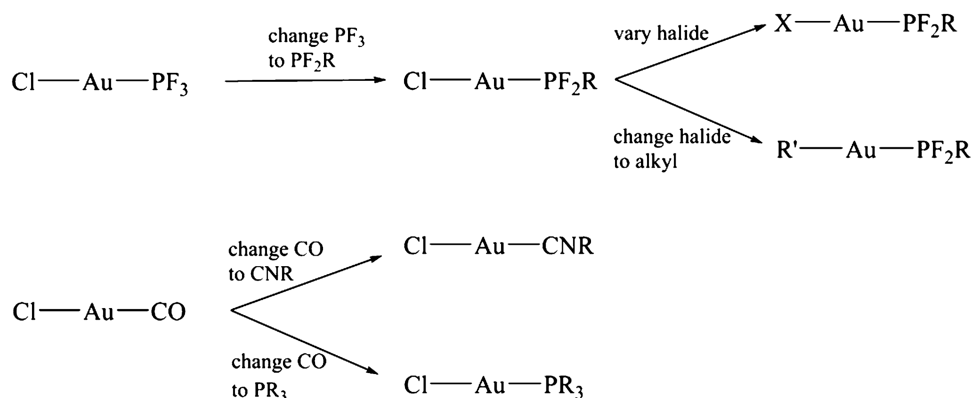

Fig. 16 Conceptual strategy for generating a library of Au(I) precursor candidates

R group is the amino-substituted complex $ClAuPF_2N(CH_3)_2$, which has a thermal decomposition temperature of 143 °C, in contrast to the decomposition of $ClAu(PF_3)$ at only 45 °C. If $ClAuPF_2R$ derivatives decompose before sufficient volatilization for EBID, the halide ligand could be varied or replaced with an alkyl group. In complexes of Br or I, the negative effects of higher molecular weight on volatility could potentially be compensated by weaker intermolecular interactions through the halides [66, 67].

The lead compounds $ClAu(PF_3)$ and ClAuCO suggest another series of precursor candidates in which the labile carbonyl ligand in ClAuCO is replaced with another π-acidic ligand (L, Fig. 16), perhaps an isocyanide. An isocyanide is isoelectronic with the CO ligand, although it is a better σ-donor, which stabilizes the analogous Au(I) complexes. The CO ligand could also be replaced by a π-basic trialkylphosphine group such as $P(CH_3)_3$. Complexes of the type $XAuPR_3$ can be easily prepared using standard Schlenk techniques and handled under ambient light [67], providing significant practical advantages if they are suitable as EBID precursors.

2.2 Strategies for Pt precursors

Using the same basic design concept of simple coordination spheres with ligands that have been shown to desorb during the deposition step or are capable of being removed by electron beam processing, four-coordinate square planar Pt(II) complexes would seem to be more attractive for EBID than $MeCpPtMe_3$, the carbon-rich pseudo-octahedral CVD precursor used in prior EBID studies [2, 23, 24]. As a potential lead compound for Pt, a reasonable candidate is $Cl_2Pt(CO)_2$ [68], which shares a common ligand set with ClAuCO. Although $Cl_2Pt(CO)_2$ has not been used in EBID, it is volatile enough to be purified by sublimation without decomposition [69] and has been used for CVD [70, 71]. Based on the existing hypothesis for the EBID reactions of ClAuCO, one potential route for $Cl_2Pt(CO)_2$ to create pure Pt deposits via EBID is through the following sequence of steps:

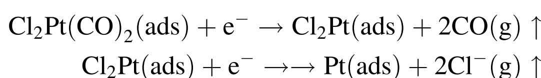

$$Cl_2Pt(CO)_2(ads) + e^- \rightarrow Cl_2Pt(ads) + 2CO(g)\uparrow$$
$$Cl_2Pt(ads) + e^- \rightarrow\rightarrow Pt(ads) + 2Cl^-(g)\uparrow$$

Like ClAu(CO), $Cl_2Pt(CO)_2$ is very water-sensitive and prone to carbonyl loss [72], so strategies similar to those described for Au precursors might well be needed to prepare other, more practically viable EBID precursors. The ligand variation scheme (Fig. 17) is analogous to the one for Au(I) complexes incorporating several known compound types, such as $PtX_2(CO)_2$ [73], $PtR_2(CO)_2$ [74], $PtR_2(PF_3)_2$ [74], and $X_2Pt(CNR')_2$ [75]. Such studies would be an important step toward developing a set of coherent design rules for EBID precursors.

3 The future

As a result of the increasing engagement of the EBID community with synthetic inorganic chemists, a number of outstanding scientific questions can also now be addressed related to the reactions of organometallic complexes with systematic structural and compositional differences. Specifically, how do organometallic precursors with:

(a) The same metal center but systematic differences in ligand architecture behave under the influence of electron irradiation? A related question is the extent to which the behavior of a particular ligand is sensitive to the surrounding architecture. For example, to what extent is the fate of the CO ligands in an organometallic complex of the general type $M(CO)_3X$ influenced by the nature of ligand X? Information from these studies will be equally useful in testing hypotheses based on studies conducted from existing precursors and also in the development of design strategies for new precursors.

(b) The same ligand architecture but different metal centers behave in EBID? Recent studies on $metal(hfac)_2$ complexes suggest that the nature of the metal center is irrelevant in determining the bond

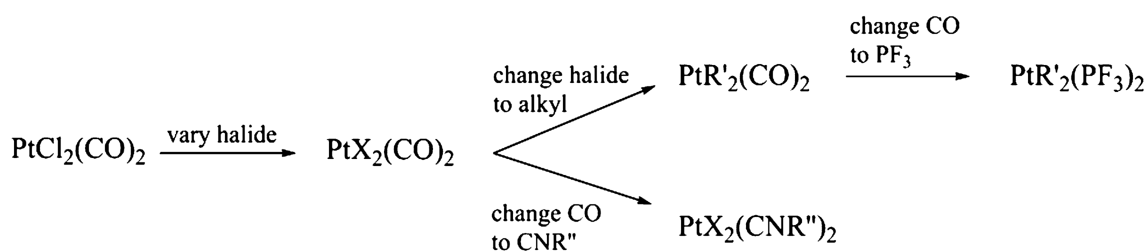

Fig. 17 Conceptual strategy for generating a library of Pt(II) precursor candidates

breaking sequence [76]. This assertion is supported by anecdotal information from gas phase studies on $Ni(PF_3)_4$ and $Pt(PF_3)_4$ which have shown that a similar DEA attachment mechanism is operative in both complexes, favoring the loss of only one of the PF_3 groups [77]. If this trend is confirmed by more surface science and electron microscopy studies on new precursors, then the behavior of one type of ligand architecture can confidently be extrapolated to other transition metals.

Although a more detailed understanding of EBID will almost certainly benefit from a wider array of customized precursors, one area where progress in the field remains slow is in the development of a more detailed theoretical, molecular level understanding of how and why organometallic precursors fragment in the way they do under the influence of electron irradiation. The difficulty lies in part due to the relative complexity of many of the organometallic complexes used in EBID and also in the need for theory to tackle molecules in electronically excited states where DFT is unreliable. However, one positive development in this area over the past several years has been the appearance of a number of gas phase studies on electron beam interactions with EBID precursors, which should serve as a less complex starting point for meaningful theoretical efforts.

4 Summary

The issue of organic contamination in EBID structures is one of the key challenges hampering the development of EBID as a robust technology for fabricating nanostructures that could otherwise have a wide array of applications in fields as diverse as catalysis, biosensing, and plasmonics. Although not complete, insights from UHV surface science studies have started to uncover some of the elementary reactions steps that underpin EBID, including a more detailed understanding of the role of ligand architecture in the deposition process. The state of knowledge has now developed to a point where organometallic chemists can begin the rational design of new precursors specifically for EBID applications. It is hoped that the close interdisciplinary collaboration between surface scientists and synthetic chemists will enable new EBID nanostructures to be created with metal contents than are significantly improved over those possible with existing CVD precursors.

References

1. S.J. Randolph, J.D. Fowlkes, P.D. Rack, Crit. Rev. Solid State Mater. Sci. **31**, 55 (2006)
2. I. Utke, P. Hoffman, J. Melngailis, J. Vac. Sci. Technol., B **26**(4), 1197 (2008)
3. W.F. van Dorp, C.W. Hagen, J. Appl. Phys. **104**, 081301 (2008)
4. M. Huth, F. Porrati, C. Schwalb, M. Winhold, R. Sachser, M. Dukic, J. Adams, G. Fantner, Beilstein J. Nanotechnol. **3**, 597 (2012)
5. L. Frey, C. Lehrer, H. Ryssel, Appl. Phys. A Mater. Sci. Process. **76**(7), 1017 (2003)
6. J.Y. Igaki, K. Kanda, Y. Haruyama, M. Ishida, Y. Ochiai, J.I. Fujita, T. Kaito, S. Matsui, Microelectron. Eng. **83**, 1225 (2006)
7. T. Fujii, K. Iwasaki, M. Muekane, T. Takeuchi, M. Hasuda, Y. Asahata, M. Kyohara, T. Kogure, Y. Kijima, T. Kaito, J. Micromech. Microeng. **15**(10), S286 (2005)
8. J.N. Helbert, *Handbook of VLSI Microlithography Principles Tools Technology and Applications*, 2nd edn. (Noyes /William Andrew Publishing, Norwich, New York 2001)
9. V. Bakshi, *EUV Lithography* (SPIE/Wiley Interscience, New York, 2009)
10. W.F. van Dorp, I. Lazic, A. Beyer, A. Gölzhāuser, J.B. Wagner, T.W. Hansen, C.W. Hagen, Nanotechnology **22**(11), 115303 (2011)
11. J. Brown, P. Kocher, C.S. Ramanujan, D.N. Sharp, K. Torimitsu, J.S. Ryan, Ultramicroscopy **133**, 62 (2013)
12. J.C. Van Oven, F. Berwald, K.K. Berggen, P. Kruit, C.W. Hagen, J. Vac. Sci. Technol., B **29**(6), 06F305 (2011)
13. A. Fernandez-Pacheco, L. Serrano-Ramón, J.M. Michalik, M.R. Ibarra, J.M. De Teresa, L. O'Brien, D. Petit, J. Lee, R.P. Coburn, Sci. Rep. **3**, 1492 (2013)
14. A. Perentes, P. Hoffmann, Chem. Vap. Depos. **13**, 176 (2007)
15. K. Edinger, H. Becht, J. Bihr, V. Boegli, M. Budach, T. Hofmann, H.W.P. Koops, P. Kuschnerus, J. Oster, P. Spies, B. Weyrauch, J. Vac. Sci. Technol., B: Microelectron. Nanometer Struct.–Process., Meas., Phenom. **22**(6), 2902 (2004)
16. T. Liang, E. Frendberg, B. Lieberman, A. Stivers, J. Vac. Sci. Technol., B: Microelectron. Nanometer Struct.–Process., Meas., Phenom. **23**(6), 3101 (2005)
17. C.Th.H. Heerkens, M.J. Kamerbeek, W.F. van Dorp, C.W. Hagen, J. Hoekstra, Microelectron. Eng. **86**, 961 (2009)
18. B. Hubner, H.W.P. Koops, H. Pagnia, N. Sotnik, J. Urban, M. Weber, Ultramicroscopy **42–44**, 1519 (1992)

19. I.-C. Chen, L.-H. Chen, C. Orme, A. Quist, R. Lal, S. Jin, Nanotechnology **17**, 4322 (2006)
20. S. Graells, R. Alcubilla, G. Badenes, R. Quidant, Appl. Phys. Lett. **91**, 121112 (2007)
21. A. Weber-Bargioni, A. Schwartzberg, M. Schmidt, B. Harteneck, D.F. Ogletree, P.J. Schuck, S. Cabrini, Nanotechnology **21**, 065301 (2010)
22. H.W.P. Koops, O.E. Hoinkis, M.E.W. Honsberg, R. Schmidt, R. Blum, G. Bottger, A. Kuligk, C. Liguda, M. Eich, Microelectron. Eng. **57–58**, 995 (2001)
23. H.W. Koops, A. Kaya, M. Weber, J. Vac. Sci. Technol., B **13**(6), 2400 (1995)
24. A. Botman, M. Hesselberth, J.J.L. Mulders, Microelectron. Eng. **85**, 1139 (2008)
25. K.L. Klein, S.J. Randolph, J.D. Fowlkes, L.F. Allard, H.M. Meyer III, M.L. Simpson, P.D. Rack, Nanotechnology **19**, 345705 (2008)
26. A. Botman, M. Hesselberth, J.J.L. Mulders, J. Vac. Sci. Technol., B **26**(6), 2464 (2008)
27. P.D. Tran, P. Doppelt, J. Electrochem. Soc. **154**(10), D520 (2007)
28. T. Brintlinger, M.S. Fuhrer, J. Melngailis, I. Utke, T. Bret, A. Perentes, P. Hoffmann, M. Abourida, P. Doppelt, J. Vac. Sci. Technol., B: Microelectron. Nanometer Struct.–Process., Meas. Phenom. **23**(6), 3174 (2005)
29. L. McElwee-White, Dalton Trans., 5327 (2006)
30. L. McElwee-White, J. Koller, D. Kim, T.J. Anderson, ECS Trans. **25**(8), 161 (2009)
31. W.F. van Dorp, J.D. Wnuk, J.M. Gorham, D.H. Fairbrother, T.E. Madey, C.W. Hagen, J. Appl. Phys. **106**, 074903 (2009)
32. J.D. Wnuk, J.M. Gorham, S.G. Rosenberg, W.F. van Dorp, T.E. Madey, C.W. Hagen, D.H. Fairbrother, J. Phys. Chem. C **113**, 2487 (2009)
33. J.D. Wnuk, J.M. Gorham, S.G. Rosenberg, W.F. van Dorp, T.E. Madey, C.W. Hagen, D.H. Fairbrother, J. Appl. Phys. **107**, 5–054301 (2010)
34. J.D. Wnuk, S.G. Rosenberg, J.M. Gorham, W.F. van Dorp, C.W. Hagen, D.H. Fairbrother, Surf. Sci. **605**, 3–4–257 (2011)
35. S.G. Rosenberg, K. Landheer, C.W. Hagen, D.H. Fairbrother, J. Vac. Sci. Technol., B **30**, 051805 (2012)
36. S.G. Rosenberg, M. Barclay, D.H. Fairbrother, Phys. Chem. Chem. Phys. **15**(11), 4002 (2013)
37. S.G. Rosenberg, M. Barclay, D.H. Fairbrother, J. Phys. Chem. C **117**(31), 16053 (2013)
38. K. Landheer, S.G. Rosenberg, L. Bernau, P. Swiderek, I. Utke, C.W. Hagen, D.H. Fairbrother, J. Phys. Chem. C **115**(35), 17452 (2011)
39. A. Perentes, G. Sinicco, G. Boero, B. Dwir, P. Hoffmann, J. Vac. Sci. Technol., B **25**, 2228 (2007)
40. M.H. Ervin, B.M. Nichols, J. Vac. Sci. Technol., B **27**(6), 2982 (2009)
41. A. Fernandez-Pacheco, J.M. De Teresa, R. Cordoba, M.R. Ibarra, J. Phys. D Appl. Phys. **42**, 055005 (2009)
42. A. Fernandez-Pacheco, J.M. De Teresa, R. Cordoba, M.R. Ibarra, D. Petit, D.E. Read, L. O'Brien, E.R. Lewis, H.T. Zeng, R.P. Cowburn, Appl. Phys. Lett. **94**, 19–192501 (2009)
43. M. Gabureac, L. Bernau, I. Utke, G. Boero, Nanotechnology **21**(11), 115501 (2010)
44. G.C. Gazzadi, H. Mulders, P. Trompenaars, A. Ghirri, M. Affronte, V. Grillo, S. Frabboni, J. Phys. Chem. C **115**(40), 19606 (2011)
45. G.C. Gazzadi, J.J.L. Mulders, P. Trompenaars, A. Ghirri, A. Rota, M. Affronte, S. Frabboni, Microelectron. Eng. **88**(8), 1955 (2011)
46. I. Sychugov, Y. Nakayama, K. Mitsuishi, J. Phys. Chem. C **113**, 21516 (2009)
47. W.F. van Dorp, B. van Someren, C.W. Hagen, P. Kruit, P.A. Crozier, J. Vac. Sci. Technol., B **24**(2), 618 (2006)
48. W.F. van Dorp, C.W. Hagen, P.A. Crozier, P. Kruit, Nanotechnology **19**, 225305 (2008)
49. F. Porrati, R. Sachser, C.H. Schwalb, A.S. Frangakis, M. Huth, J. Appl. Phys. **109**, 063715/1 (2011)
50. S. Frabboni, G.C. Gazzadi, L. Felisari, A. Spessot, Appl. Phys. Lett. **88**, 213116 (2006)
51. S. Frabboni, G.C. Gazzadi, A. Spessot, Phys. E **37**, 265 (2007)
52. P.D. Rack, S. Randolph, Y. Deng, J. Fowlkes, Y. Choi, D.C. Joy, Appl. Phys. Lett. **82**, 14–2326 (2003)
53. S. Engmann, M. Stano, Š. Matejčík, O. Ingólfsson, Phys. Chem. Chem. Phys. **14**, 14611 (2012)
54. J. Barry, M.H. Ervin, J. Molstad, A. Wickenden, T. Brintlinger, P. Hoffman, J. Meingailis, J. Vac. Sci. Technol., B **24**(6), 3165 (2006)
55. A. Botman, C.W. Hagen, J. Li, B.L. Thiel, K.A. Dunn, J.J.L. Mulders, S.J. Randolph, M. Toth, J. Vac. Sci. Technol., B **27**(6), 2759 (2009)
56. M. Takeguchi, M. Shimojo, K. Furuya, Appl. Phys. A Mater. Sci. Process. **93**, 439 (2008)
57. S. Wang, Y.-M. Sun, Q. Wang, J.M. White, J. Vac. Sci. Technol., B **22**(4), 1803 (2004)
58. O. May, D. Kubala, M. Allan, Phys. Chem. Chem. Phys. **14**, 2979 (2012)
59. M.H. Ervin, D. Chang, B. Nichols, A. Wickenden, J. Barry, J. Melngailis, J. Vac. Sci. Technol., B **25**(6), 2250 (2007)
60. J.J.L. Mulders, L.M. Belova, A. Riazanova, Nanotechnology **22**(5), 055302/1 (2011)
61. J.J.L. Mulders, J.M. Veerhoek, E.G.T. Bosch, P.H.F. Trompenaars, J. Phys. D Appl. Phys. **45**, 47–475301/1 (2012)
62. W. Fuss, M. Ruehe, Z. Naturforsch., B: Chem. Sci. **47**, 591 (1992)
63. F. Schödel, M. Bolte, M. Wagner, H.-W. Lerner, Z. Anorg. Allg. Chem. **632**, 4–652 (2006)
64. D. Woska, A. Prock, W.P. Giering, Organometallics **19**, 4629 (2000)
65. A. Graefe, T. Kruck, J. Organomet. Chem. **506**, 31 (1996)
66. R. Heathcote, J.A.S. Howell, N. Jennings, D. Cartlidge, L. Cobden, S. Coles, M. Hursthouse, Dalton Trans. **13**, 1309 (2007)
67. F.G. Mann, A.F. Wells, D. Purdie, J. Chem. Soc. (Resumed) **0**, 1828 (1937)
68. D.B. Dell'Amico, L. Labella, J. Organomet. Chem. **593–594**, 427 (2000)
69. B. von Ahsen, R. Wartchow, H. Willner, V. Jonas, F. Aubke, Inorg. Chem. **39**, 4424 (2000)
70. J.R. Vargas Garcia, T. Goto, Mater. Trans. **44**, 9–1717 (2003)
71. R.M. Guerrero, J.R. Vargas Garcia, V. Santes, E. Gomez, J. Alloys Compd. **434–435**, 701 (2007)
72. M.J. Rand, J. Electrochem. Soc. **120**, 5–686 (1973)
73. F. Bagnoli, D.B. Dell'Amico, F. Calderazzo, U. Englert, F. Marchetti, A. Merigo, S. Ramello, J. Organomet. Chem. **622**, 180 (2001)
74. R. Friedemann, K. Seppelt, Eur. J. Inorg. Chem. **2013**, 1197 (2013)
75. J. Browning, P. L. Goggin, R. J. Goodfellow, J. Chem. Res. (S), 328 (1978)
76. S.G. Rosenberg, M. Barclay, D.H. Fairbrother, ACS Appl. Mater. Interfaces **6**, 8590–8601 (2014)
77. J.F. Friedman, T.M. Miller, J.K. Friedman-Schaffer, A.A. Viggiano, G.K. Rekha, A.E. Stevens, J. Chem. Phys. **104303**, 128 (2008)